J. Fluid Mech. (2024), *vol*. 995, A6, doi:10.1017/jfm.2024.680

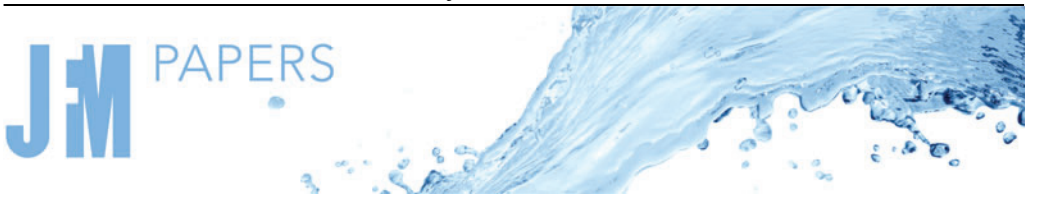

Detachment of leading-edge vortex enhances wake capture force production

Hao Li[1],† **and Mostafa R.A. Nabawy**[1,2],†

[1]School of Engineering, The University of Manchester, Manchester M13 9PL, UK

[2]Aerospace Engineering Department, Faculty of Engineering, Cairo University, Giza 12613, Egypt

(Received 14 November 2023; revised 3 June 2024; accepted 17 July 2024)

During stroke reversals, insect wings interact with their own wake flow from the preceding half-stroke, resulting in an unsteady aerodynamic mechanism known as 'wing–wake interaction' or 'wake capture'. To better elucidate this mechanism, we numerically solved the incompressible Navier–Stokes equations at Reynolds numbers 10^2 and 10^3. Simulations were conducted for wing planforms defined using the beta function distribution with varying aspect ratios ($AR = 2$–6) and radial centroid locations ($\hat{r}_1 = 0.4$–0.6), whilst employing representative normal hovering kinematics. The wake development from the considered flapping wing planforms was investigated, and the wake capture contribution to aerodynamic force production was quantified by comparing the force generation between the fifth and first stroke cycles at multiple sections along the wingspan. Our results revealed that on the inboard wing region experiencing an attached leading-edge vortex (LEV) structure, wing–wake interaction is dominated by an unsteady downwash effect, resulting in a reduction in local force production. However, in regions closer to the wingtip experiencing detachment of the LEV, wing–wake interaction is dominated by an unsteady upwash effect, leading to an increase in local force production. Consequently, the global wake capture force production is controlled by the extent of LEV detachment, which primarily increases with the increase of wing aspect ratio. This suggests that for normal hovering flapping wings, the typical loss in translational force production due to wingtip stall is partially mitigated by wake capture effects.

Key words: swimming/flying, separated flows

† Email addresses for correspondence: hao.li@manchester.ac.uk, mostafa.ahmednabawy@manchester.ac.uk

1. Introduction

Wake capture is an unsteady aerodynamic mechanism that emerges when a flapping wing flips direction, interacting with the region of disturbed air, i.e. wake, left behind from the preceding half-stroke. This mechanism exerts a significant influence on the flow structures encountered during the subsequent flapping half-stroke, thereby providing a substantial impact on the production of aerodynamic forces. Despite its significance, wake capture remains a relatively under-explored aspect of flapping wing aerodynamics. In fact, presently, there is lack of consensus regarding its underlying physics, insufficient dedicated experimental and numerical data, and a near absence of comprehensive theoretical models.

Wake capture in flapping wings was first explored experimentally by Dickinson & Götz (1993), employing a two-dimensional (2-D) aerofoil subjected to sequential translation, pitching and reverse translation motions. This early work demonstrated that wake capture can lead to a momentary peak in lift during the reverse half-stroke. Building upon this, a subsequent study by Dickinson, Lehmann & Sane (1999) employed a more sophisticated robotic apparatus to scrutinise the impact of wake capture on force generation of three-dimensional (3-D) fruit fly model wings. They abruptly halted the wing's motion at the culmination of a half-stroke, showcasing that wake interactions can lead to favourable or detrimental effects depending on how advanced or delayed is the pitching motion relative to the flapping motion. Later, Birch & Dickinson (2003) investigated the wake structure of the same flapping fruit fly model wings using particle image velocimetry. They pinpointed a pair of residual vortices generating a high-velocity jet impinging the wing's lower surface, initially bolstering lift followed by a subsequent decay in lift, which was attributed to downwash effects. Computational models have also been employed early on to investigate wake capture, and notably the work of Sun & Tang (2002) involved comparison of force production by a flapping fruit-fly-like wing in two scenarios: one in which it operated in still air devoid of wake effects, and the other in fully developed wake conditions. Their results revealed no appreciable increase in lift due to wake capture, in contrast to the findings of Dickinson *et al.* (1999). This disagreement led to a vigorous debate within the community that later created some sort of stagnation in studying wake capture.

Nevertheless, in recent years, interest in wake capture has renewed, driven primarily by the discussed lack of consensus on its physical explanation. Notably, Lee & Lua (2018) conducted a comparative study of wake capture effects between 2-D and 3-D flapping wings through numerical simulations. They showed that the lift enhancement resulting from wake capture gradually diminishes as the wing motion transitions from 2-D to 3-D. Furthermore, when wing aspect ratio drops below 4, wake capture yields no lift enhancement. In a more recent endeavour, Li & Nabawy (2022*a*) employed numerical simulations to explore the aerodynamics of wake capture within 2-D flows. They set up a flat plate to interact with its wake whilst travelling stroke distances ranging between 2 and 6, which aligns with the range of typical stroke distances observed for natural insect wings when measured at the radius of gyration (Ellington 1984*a*,*b*). Their findings revealed that beneficial lift enhancement due to wake interactions is contingent on specific stroke distances that lead to a detached leading-edge vortex (LEV). This underscores the critical importance of the LEV structure in determining the impact of wake capture effects.

To date, wake capture may still be seen as a mystery in flapping wing aerodynamics. In fact, studies conducted so far have failed to reveal a consistent trend when evaluating the wake's influence on the overall force production. This inconsistency can be attributed to the substantial spanwise variations within the wake of a flapping wing. Notably, these variations are closely linked to the LEV structure, which is known to undergo

distinct changes along the wingspan. The variations in the LEV structure not only lead to a modulation of the force distribution during wing translation (Phillips, Knowles & Bomphrey 2015; Li & Nabawy 2022*c*) but are also expected to have a profound influence on the interaction between the wing and its wake. Remarkably, despite its significance, this latter aspect has always been overlooked in the literature. As such, in this study, we thoroughly examined the flow and force coefficients at distinct spanwise positions across a comprehensive range of wing planforms. This examination led, for the first time, to a comprehensive characterisation of the spatial and temporal effects of wake capture for the representative normal hovering insect-like kinematics considered in this work.

2. Problem description and methodology

In the current study, rigid wings are considered with planform shapes defined using the beta function distribution. This distribution is known to provide a close representation of real insect wing shapes (Ellington 1984*a*). The chord length distribution along the wingspan is given by (Ellington 1984*a*):

$$\hat{c}(\hat{r}) = \frac{c(\hat{r})}{\bar{c}} = \frac{\hat{r}^{p-1}(1-\hat{r})^{q-1}}{\displaystyle\int_0^1 \hat{r}^{p-1}(1-\hat{r})^{q-1}\,\mathrm{d}\hat{r}}, \quad p = \hat{r}_1\left[\frac{\hat{r}_1(1-\hat{r}_1)}{\hat{r}_2^2-\hat{r}_1^2}-1\right], \quad q = p\left[\frac{(1-\hat{r}_1)}{\hat{r}_1}\right], \tag{2.1a–c}$$

where $\hat{r}$ is the radial position normalised using the unilateral wingspan R, and the non-dimensional radii of the first and second moments of wing area, $\hat{r}_1$ and $\hat{r}_2$, are further related as $\hat{r}_2 = 0.929\,\hat{r}_1^{0.732}$ (Ellington 1984*a*). The aspect ratio (AR) values are varied between 2 and 6, with a unity step increment. For each aspect ratio, three radial centroid locations $\hat{r}_1 = 0.4$, 0.5 and 0.6 are considered. These values ensure that most insect wing morphologies are covered in our study, based on the data provided by Ellington (1984*a*). For all cases, the wing thickness is set to 5 % of the mean chord length, $\bar{c} = R/AR$, and the axis of pitching rotation is fixed at the quarter-chord line from the leading edge (Broadley *et al.* 2022). Figure 1 shows the 15 wing planform shapes investigated in this study.

Lift-based 'normal hovering' kinematics are employed in this study. The equations used to model the variations of the flapping (ϕ) and pitching (θ) angles are (Berman & Wang 2007; Nabawy & Crowther 2015)

$$\phi(\hat{t}) = \frac{\phi_{max}}{\sin^{-1} C_\phi}\sin^{-1}\left[C_\phi\cos(2\pi\hat{t})\right], \tag{2.2}$$

$$\theta(\hat{t}) = \frac{\theta_{max}}{\tanh C_\theta}\tanh\left[C_\theta\sin(2\pi\hat{t})\right], \tag{2.3}$$

where $\hat{t}$ is the normalised time with respect to the flapping stroke period. The flapping angle amplitude is chosen as $\phi_{max} = 70^\circ$, corresponding to a stroke peak-to-peak amplitude 140°, a mean value of the representative insect data reported by Sun & Du (2003). The maximum pitch angle of the wing is set to $\theta_{max} = 45^\circ$, allowing a mid-half-stroke angle of attack value 45°, known to produce the highest lift coefficient values. Note that for the kinematics employed in this study, the angle of attack can be simply evaluated as $\alpha(t) = (\pi/2) - |\theta(t)|$ (Nabawy & Crowther 2015). Care was taken to ensure that the waveform time variations are practically realistic through smooth transitions at stroke reversals whilst simultaneously being able to maximally expose wake capture effects via adopting near-constant flapping velocity and angle of attack profiles at

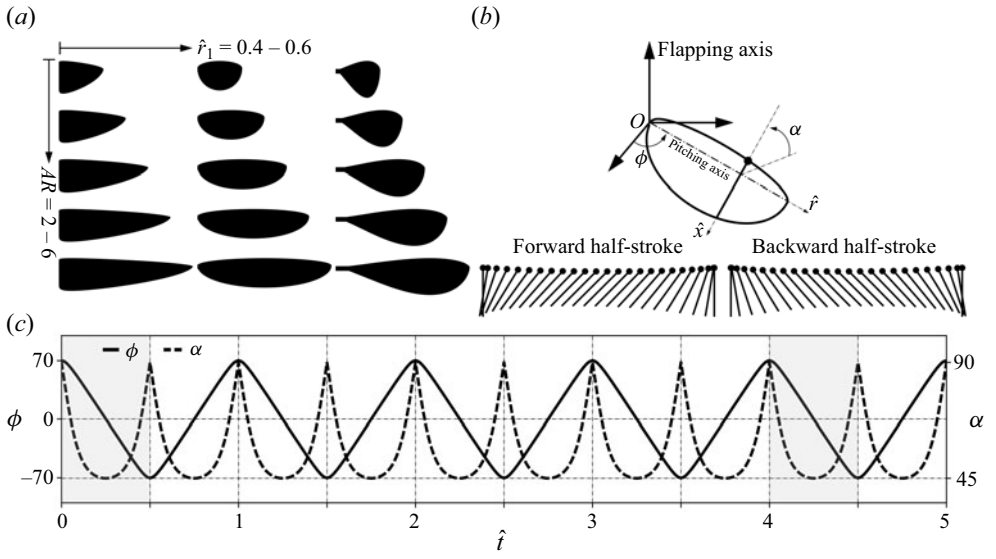

Figure 1. Wing planform shapes and kinematic waveforms employed in this study. The forward half-strokes of the first and fifth cycles are marked in grey.

mid-half-strokes (Nabawy 2023). As such, we employed a C_ϕ value 0.97 and a C_θ value 1.6 to enable such waveform requirements (figure 1).

The lift and drag coefficients C_L and C_D are defined based on the average translational velocity of the wing at the radius of the second moment of wing area, U_2:

$$C_L(\hat{t}) = \frac{L(\hat{t})}{0.5\,\rho U_2^2 S}, \quad C_D(\hat{t}) = \frac{D(\hat{t})}{0.5\,\rho U_2^2 S}, \tag{2.4a,b}$$

where L, D are the lift and drag forces, and S is the wing area. Additionally, the spanwise distribution of the aerodynamic force is assessed using the force coefficients at distinct wing sections along the wingspan. For the flat wings considered in this study, it is convenient to use only the aerodynamic force component normal to the wing surface in this assessment. This is because the tangential viscous contribution accounts for less than 2 % of the overall aerodynamic force in all cases examined, hence can be neglected. The normal force coefficient C_n for a wing section at a spanwise location $\hat{r}$ and non-dimensional time $\hat{t}$ is obtained using the equation

$$C_n(\hat{r}, \hat{t}) = \frac{\displaystyle\int_0^{\hat{c}(\hat{r})} \left[p_l(\hat{x}, \hat{t}) - p_u(\hat{x}, \hat{t})\right] \mathrm{d}\hat{x}}{0.5\,\rho U_2^2}, \tag{2.5}$$

where $\hat{c}$ is the local chord length normalised using the mean chord length (see (2.1*a–c*)), and $p_{l/u}$ is the pressure on the lower/upper wing surface at a local chordwise coordinate normalised using the mean chord length $\hat{x} = x/\bar{c}$ and normalised time $\hat{t}$. The reference velocity (U_2) values were set to enable specific mean-chord-based Reynolds number values, specifically 10^2 and 10^3, being representative of the flights of insects scaling from flies up to bees.

Flows around the flapping wings are governed by the incompressible Navier–Stokes equations:

$$\nabla \cdot \boldsymbol{u} = 0, \tag{2.6}$$

$$\frac{\partial \boldsymbol{u}}{\partial t} + \boldsymbol{u} \cdot \nabla \boldsymbol{u} = -\frac{1}{\rho} \nabla p + \nu \nabla^2 \boldsymbol{u}, \tag{2.7}$$

where $\boldsymbol{u}$ is the fluid velocity, p is the pressure, and ρ is the density. The equations are solved using the package open-source field operation and manipulation (OpenFOAM) based on a finite volume method. A spherical domain with radius $40\bar{c}$ is used for computations and is deemed adequate based on our convergence assessment for various domain sizes. The wing is positioned at the centre of this computational domain. At the spherical boundary, a Neumann condition is prescribed. Second-order schemes are utilised for both spatial and temporal discretisation. The pressure-implicit with splitting of operators for pressure linked equations (PIMPLE) algorithm (Issa 1986; Patankar & Spalding 1972) is used to solve the pressure–velocity coupling.

As for the mesh set-up, a computational hexahedral mesh is generated using the snappyHexMesh utility within OpenFOAM. A multi-level subdivision refinement is implemented for cells close to the wing surface, followed by addition of final layers to ensure cell alignment with the boundary of the wing geometry. This meshing process resulted in a mesh size between 1 and 7.6 million, depending on the wing planform shape and Reynolds number, and a typical cell spacing of less than 0.5 % of the mean chord length in all three dimensions near the wing surface. A constant time step size 10^{-3} has been employed for all simulations in the current study. More details on the computational set-up, convergence assessment and extensive validations of our numerical solver against well-known benchmark flapping wing cases were presented comprehensively in our previous works (Li & Nabawy 2022*c*,*b*), hence are not repeated here.

Figure 2 shows the lift and drag coefficients at both Reynolds numbers simulated for different aspect ratio wings with $\hat{r}_1 = 0.5$. Results presented are for the forward half-stroke of the first cycle, the fifth cycle, and the difference between these two cycles, i.e. force coefficients due to wake capture. It is evident that the force coefficient values in the first cycle are not affected by the initial conditions of the simulations. This is due to the relatively low Reynolds numbers considered in the current study: any disturbances due to initial conditions were quickly dissipated due to viscous effects. In fact, in all our simulation cases, disturbances disappeared within the first few time steps. Note that further detailed discussions on the associated normal force variation trends will follow later, in the results section.

In order to determine quantitatively the attachment state of the LEV, we evaluated its circulation on the wing upper surface at different spanwise locations. The method follows from several theoretical and experimental studies describing the detachment process for LEV on an aerofoil surface (Baik *et al.* 2012; Rival *et al.* 2014). Typically, as the LEV is formed on the upper surface, the flow surrounding the LEV boundary creates a closed recirculation region. When the LEV starts to grow in size, the flow reattachment location moves towards the trailing edge due to the extension of the recirculation region. Once the reattachment point reaches the trailing edge, the detachment of the LEV becomes inevitable. This observation suggests that the growth of the LEV is limited by the local chord length, and that the detachment of the LEV can be determined by such a characteristic length scale (Rival *et al.* 2014). Hence we employed a square interrogation window with edge length equal to the local chord length to evaluate the LEV circulation

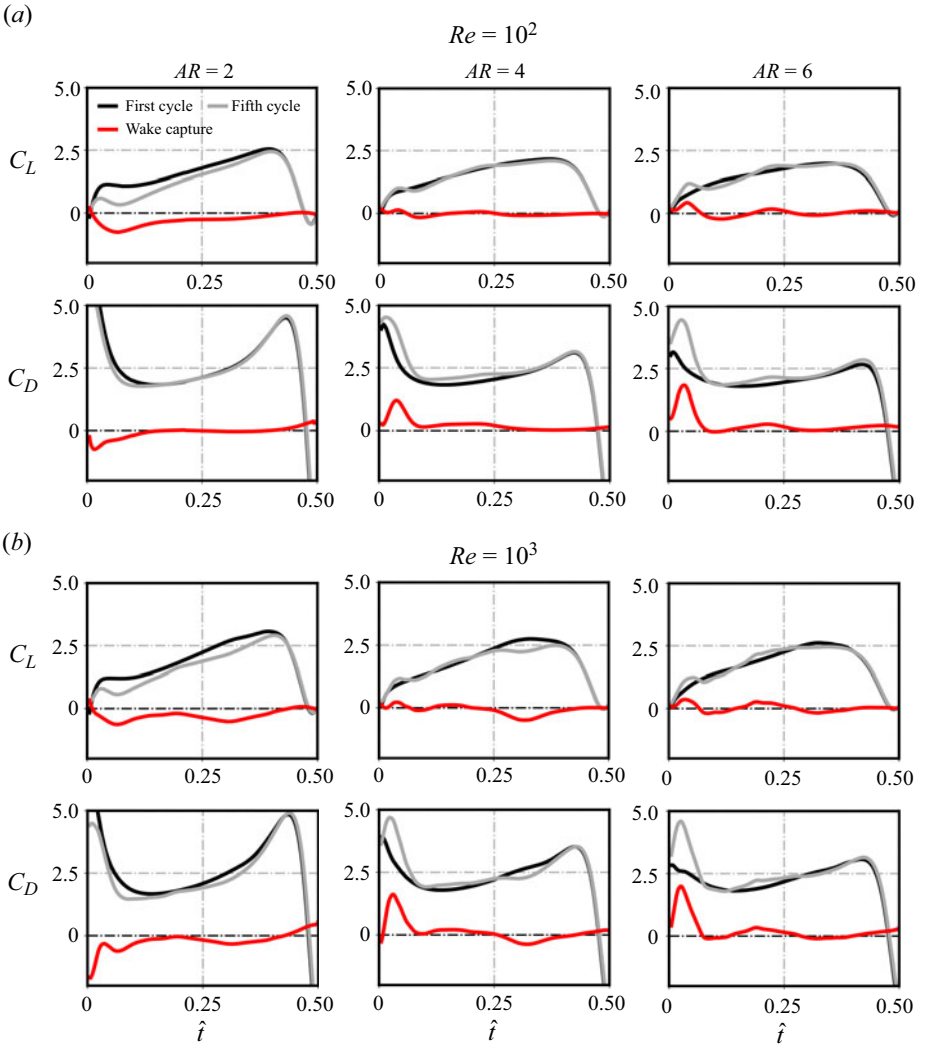

Figure 2. Lift and drag coefficients for the first cycle, fifth cycle and wake capture for wings with different aspect ratios and $\hat{r}_1 = 0.5$ at $Re = 10^2$ and 10^3.

at each wing section; see figures 3(*a*,*b*). The interrogation window aligns with the wing leading edge and has normal gap distance $0.01\bar{c}$ from the wing upper surface. For each section, the vortex structures were identified using the Q-criterion (Hunt, Wray & Moin 1988), as illustrated in figures 3(*a*,*b*). The LEV circulation within the window area was obtained by integrating the spanwise vorticity within the LEV. Note that for this assessment, a sensitivity analysis of the effect of employing different normal gap distances (between wing surface and interrogation window) ranging between $0.005\bar{c}$ and $0.02\bar{c}$ was conducted, and results showed minor differences in the circulation variation trend.

Examples of the evaluated circulations at the different spanwise locations of the wing planform with $AR = 4$ and $\hat{r}_1 = 0.5$ are shown in figures 3(*c*,*d*). We used 20 spanwise sections ranging between radial positions at 10 %–90 % of the wingspan to determine the LEV detachment location. In this assessment, sections that show a steadily growing

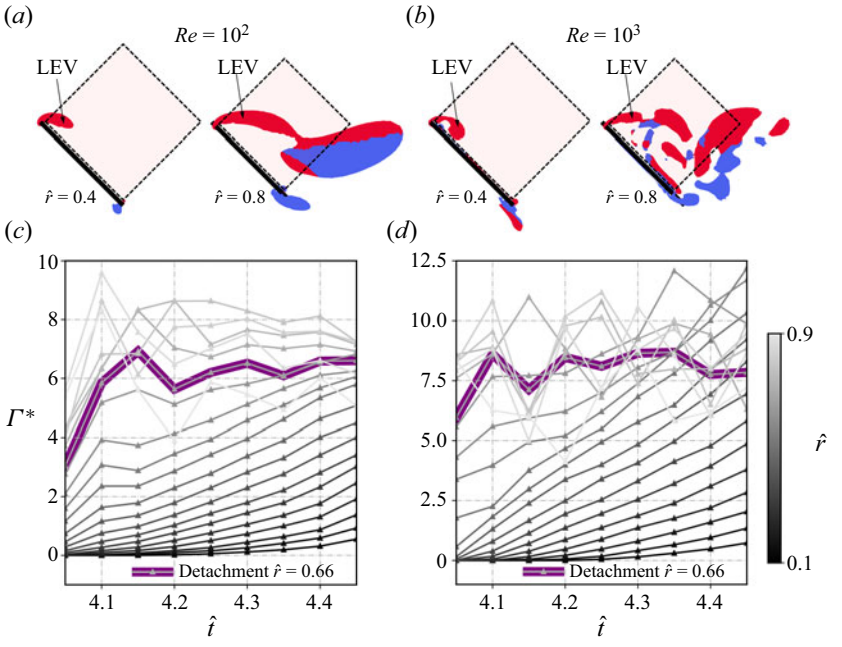

Figure 3. (*a*,*b*) Illustration of the circulation assessment interrogation window at two representative wing sections of the inboard and outboard wing regions for an example wing with $AR = 4$ and $\hat{r}_1 = 0.5$ at $Re = 10^2$ and 10^3. Vortex structures shown are for the time instance at mid-half-stroke ($\hat{t} = 4.25$). (*c*,*d*) Examples of the evaluated circulation variations at different spanwise locations for the example wing at $Re = 10^2$ and 10^3. Circulation is normalised as $\Gamma^* = \Gamma/\bar{c}U_2$.

circulation behaviour throughout a flapping half-stroke were deemed to host an attached LEV structure, whereas sections showing either sudden drop or fluctuations in the circulation values throughout the half-stroke were deemed to experience detachment and shedding of the LEV. Note that this circulation assessment directly reflects the strength of the LEV, and figures 3(*c*,*d*) clearly show that generally this strength increases from the wingroot to the wingtip regions. However, this increase tends to plateau when the LEV starts to approach breakdown/detachment from the wing surface at the outboard wing region.

3. Results and discussion

3.1. *Wake structures and velocity fields*

First, flow structures are showcased in figure 4, where the vortical structures are identified using the well-known Q-criterion (Hunt *et al.* 1988). Figures 4(*a*,*b*) showcase the fully developed wake structures on representative wing planforms, at the beginning of the fifth flapping cycle ($\hat{t} = 4.0$), for both Reynolds numbers ($Re = 10^2$ and 10^3). Figures 4(*c*,*d*) showcase a comparison of the flow structures for the forward half-stroke of the first and fifth cycles for the wing planform with $AR = 4$ and $\hat{r}_1 = 0.5$. These demonstrations provide a clear view of the spanwise variations of the wake flow structures across different wing planforms, thus laying the groundwork for subsequent discussions on sectional flows and forces. The shown wing planforms in figures 4(*a*,*b*) encompass three different aspect ratios, namely $AR = 2$, 4 and 6, all with a non-dimensional radial centroid location 0.5.

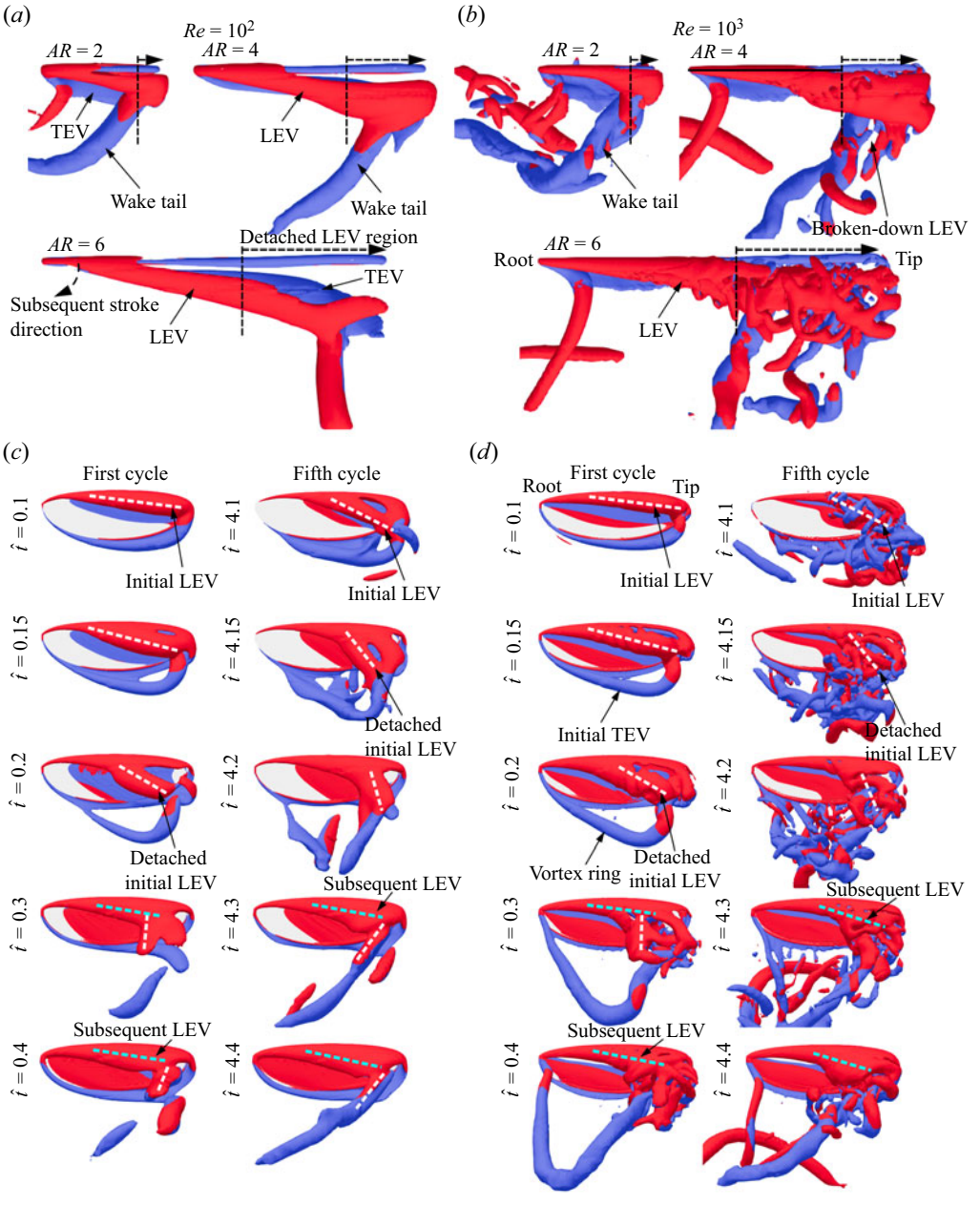

Figure 4. (*a*,*b*) Top-down perspective of wake structures at start of the fifth flapping cycle for different aspect ratio wings at $Re = 10^2$ and 10^3. (*c*,*d*) Comparison of the flow structures for the first and fifth cycles for the $AR = 4$ and $\hat{r}_1 = 0.5$ wing case at $Re = 10^2$ and 10^3. Red/blue colour indicates spanwise/anti-spanwise rotating vortices. The initial/subsequent LEV core is marked schematically with a white/cyan dashed line.

At stroke reversal, the wake produced by the flapping wing, regardless of its aspect ratio, generally comprises three distinct components: an LEV, a trailing-edge vortex (TEV), and a wake tail. Specifically, the LEV has a cone shape whose base is towards the wingtip, whereas the TEV tends to be more of a tube-like shape. Both structures tend to stay closer to the wing surface near the wingroot, but raise to a larger distance from the wing surface

towards the wingtip. For the low Reynolds number case ($Re = 10^2$), the LEV is coherent along the wingspan; however, it becomes more diffused in the wake away from the wing surface. On the other hand, for the high Reynolds number case ($Re = 10^3$), the LEV breaks down on the outboard wing region close to the wingtip, and shedding of the LEV is clearly visible in the wake behind the LEV detachment region. Note that similar LEV structures, for both low and high Reynolds number cases, have been reported in many studies of flapping wings (Jones & Babinsky 2011; Phillips *et al.* 2015), and are also commonly found in revolving wings (Harbig, Sheridan & Thompson 2013; Jardin 2017). The TEV, on the other hand, results from wing pitching rotation during stroke reversal, whereas the wake tail is, in fact, the residual part of the vortex ring structure formed by the connections between the LEV, the initial TEV and the tip vortex. It is composed primarily of the tip vortex, however, it is clearly under the influence of the interactions due to the shedding of the LEV. In fact, the evolution of the wake tail can be seen clearly in figures 4(*c*,*d*).

A notable feature between the flow development for the different cycles can be seen in figures 4(*c*,*d*), where the LEV shows a more rapid development on the outboard wing region within the fifth cycle when compared to the first cycle. Particularly for the fifth cycle, the initial LEV develops quickly and then detaches at $\hat{t} = 4.1$ for both Reynolds numbers. This can be seen clearly from the low Reynolds number case, where the detachment is marked by a split in the iso-surface for LEV structures. For the high Reynolds number case, the detachment of the initial LEV is also visible, despite being obscured by the broken-down wake vortices from the preceding half-stroke (blue iso-surfaces near the initial LEV core). On the other hand, for the first cycle, the detachment of the initial LEV is delayed to $\hat{t} = 0.15$–0.2 for both Reynolds numbers (see also later figure 9 for a similar demonstration using 2-D sectional flows). Note that in both cases, the detached initial LEV, when advected downstream into the wake, appears to be rotated with its inner end pinned to the wing surface (see rotation pattern of dashed lines in figures 4*c*,*d*), and ultimately feeds into the wake tail as time progresses. Following the detachment of the initial LEV, a subsequent LEV is formed on the wing surface, and its development is found to extend until the end of the flapping half-stroke.

The demonstrations from figures 4(*a*,*b*) and 4(*c*,*d*) show that the wake structures has a clear dependence on the spanwise position: as the distance from the wingroot increases, the wake vortex structures become increasingly more detached from the wing surface, including both the LEV and TEV. This is particularly evident for the lower Reynolds number cases ($Re = 10^2$). For the higher Reynolds number cases ($Re = 10^3$), the LEV and TEV additionally lose stability and break down at the outboard wing region. This loss of stability results in significant entrainment and mixing of the wake vortices. Such a flow picture is not new, and in fact has been reported before in several experimental studies of both flapping (Phillips *et al.* 2015) and revolving (Harbig *et al.* 2013; Kruyt *et al.* 2015) wings; however, it is reiterated here to serve as a starting point for our more detailed discussions on the wake capture mechanism.

The previous demonstration clearly showcases the distinct wake flow structures between the attached and detached LEV regions along the wingspan. To achieve a more comprehensive understanding of the wake velocity field, we present in figures 5 and 6 the sectional wake flows at $\hat{r} = 0.4$ and 0.8, representative of wing sections within the inboard and outboard wing regions, subject to attached and detached LEV structures, respectively. The wing planform shapes showcased in these demonstrations include wings with varying AR of 2, 4 and 6, and $\hat{r}_1$ value 0.5, in figure 5, and wings with $AR = 4$ but differing $\hat{r}_1$ values 0.4, 0.5 and 0.6 in figure 6. It is evident that the wake flows for the inboard and outboard wing sections exhibit clearly distinct structures, primarily in two aspects.

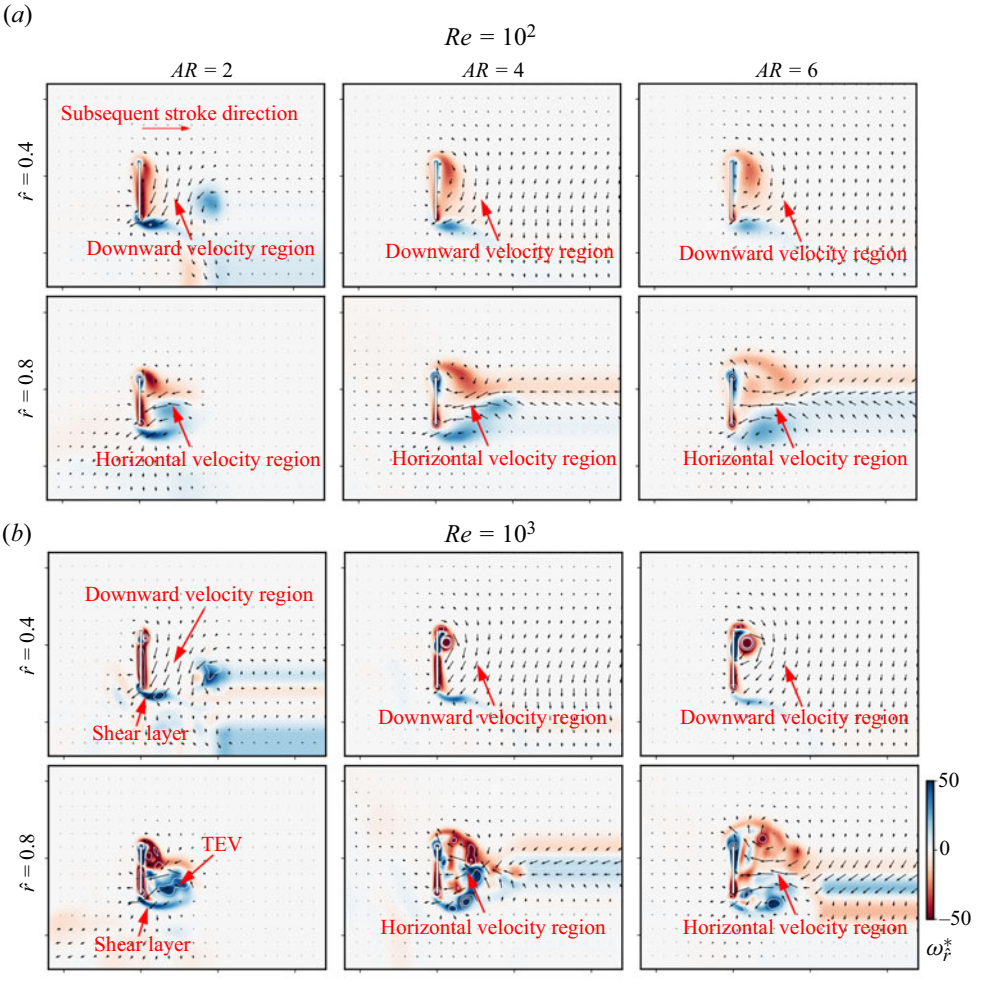

Figure 5. Sectional wake flows at the start of the fifth cycle within the inboard and outboard regions for different aspect ratio wings at $Re = 10^2$ and 10^3.

First, within the inboard wing section ($\hat{r} = 0.4$), the LEV remains in close proximity to the wing surface, while for the wing section near the wingtip ($\hat{r} = 0.8$), the LEV generally becomes detached from the wing surface. This detachment aligns consistently with the 3-D flow patterns showcased in figures 4(*a*,*b*). Second, across all aspect ratios and for both Reynolds numbers, the wake flow for the inboard wing sections form a downward velocity region trailing behind the wing, whereas within the outboard wing sections, a horizontal velocity region directed towards the wing surface is evident. These wake velocity fields are referred to as unsteady downwash and unsteady upwash, respectively. Their effects share a resemblance to the induced velocity effects that are well known within the classical rotors and propellers aerodynamics domain. However, in the current flapping wing scenario, these effects clearly have an unsteady nature, due to temporal variations associated with wing–wake interactions.

Notably, as one moves from the attached to the detached LEV region, the shear layer from the trailing edge rolls up into a more coherent TEV, occupying a larger portion near the trailing edge. The induced velocity for the combined detached LEV–TEV system on

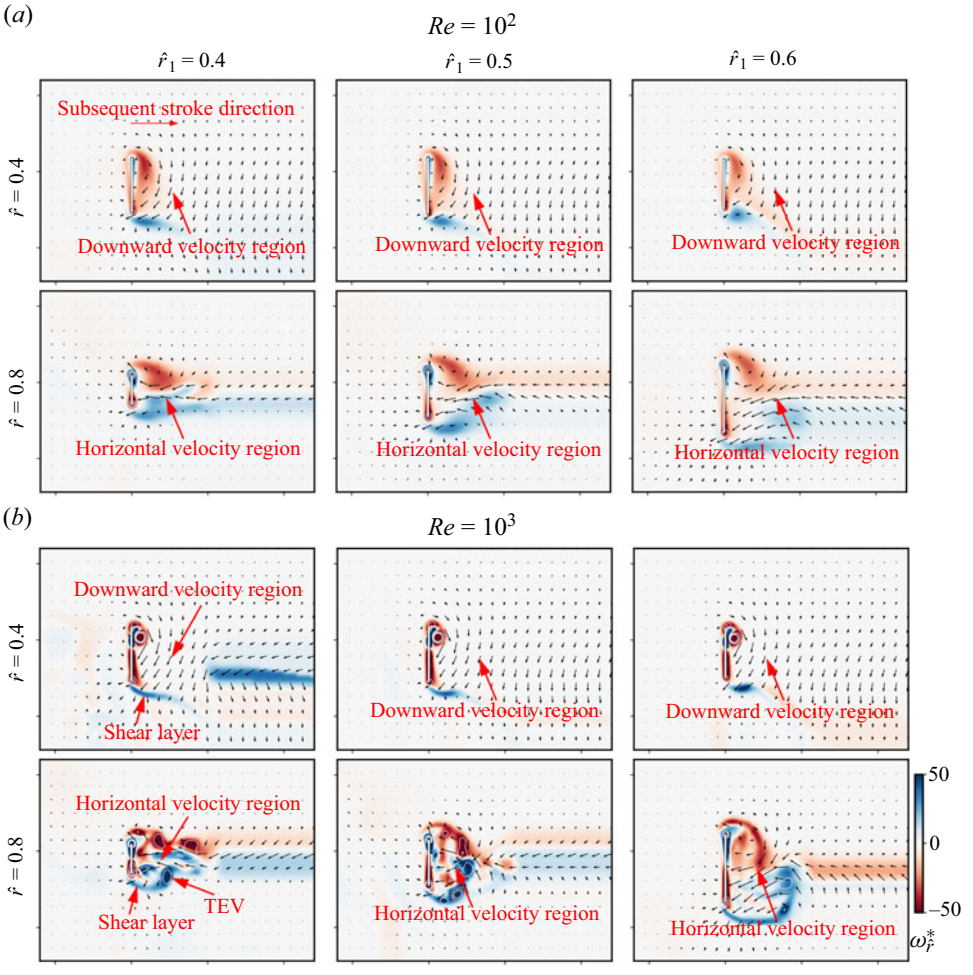

Figure 6. Sectional wake flows at the start of the fifth cycle within the inboard and outboard regions for wings with different centroids at $Re = 10^2$ and 10^3.

the outboard wing section produces a strong momentary upwash effect. This phenomenon is often referred to as 'jet impingement' in the literature (Dickinson *et al.* 1999). It should be noted here that the emergence of the TEV within the detached LEV region is, in fact, in line with the topological picture described in Rival *et al.* (2014), where the separation of the LEV leads to the opening of a channel for reverse flow, which is necessary for the subsequent development of the TEV. To complement the preceding observations, figure 7 further showcases the 3-D flow vector fields at the representative spanwise locations, i.e. $\hat{r} = 0.4$ and 0.8, just after the beginning of the fifth half-stroke ($\hat{t} = 4.05$). For a more convenient representation, cylindrical sections within the flow domain consistent with the wing's translational trajectory were employed. This demonstration provides a clear visual aid to illustrate the unsteady downwash/upwash effect experienced by the inboard/outboard wing section at the beginning of a flapping half-stroke and as the wing travels backwards through the wake-induced velocity field.

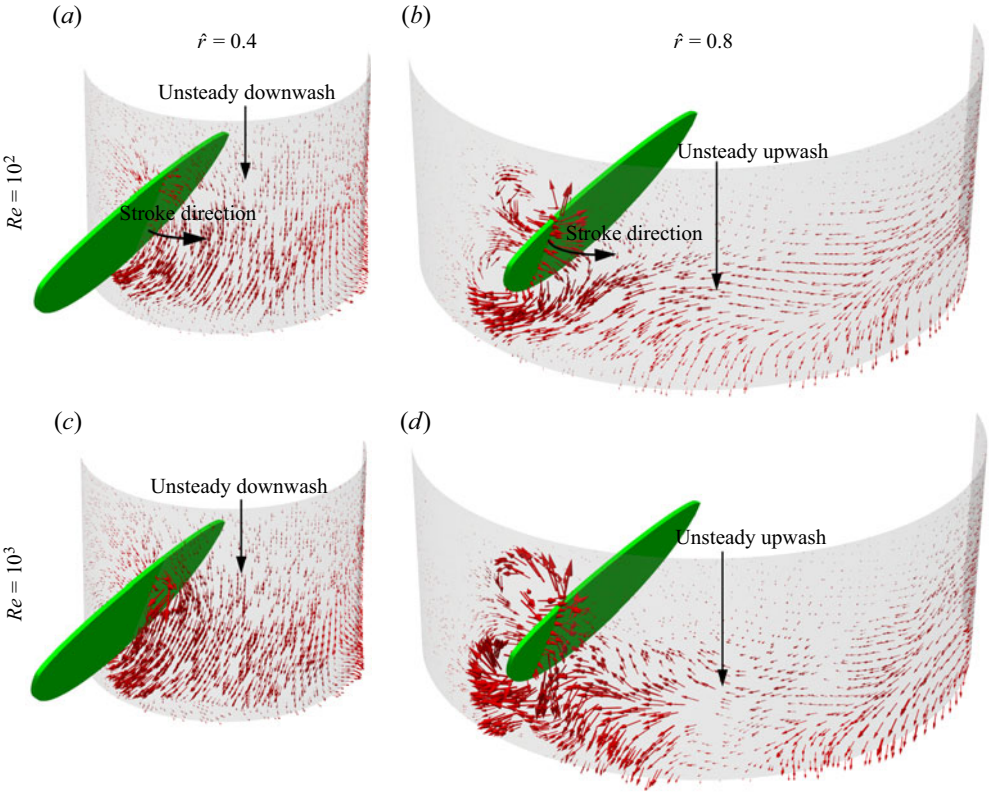

Figure 7. Wake-induced velocity fields for representative inboard and outboard wing sections just after the start of the fifth half-stroke ($\hat{t} = 4.05$) for the $AR = 4$ and $\hat{r}_1 = 0.5$ wing at $Re = 10^2$ and 10^3.

3.2. *Wake capture force production*

The aerodynamic force production due to wing–wake interaction is presented in this subsection. First, the wake capture normal force coefficients are evaluated for wing planform shapes with different AR and $\hat{r}_1$. This follows the typical procedure of contrasting the normal force coefficients of the fifth cycle encompassing fully developed wake effects, to those of the first cycle experiencing no wake effects. Note that this method of assessing the wake capture contribution has been utilised in both experimental and numerical investigations in the literature (Sun & Tang 2002; Birch & Dickinson 2003). Figure 8 shows the wake capture normal force coefficients (ΔC_n) normalised by the average normal force coefficients of the fifth cycle ($\bar{C}_n$), for the various wing planform shapes. For this demonstration, multiple wing sections at spanwise locations ranging from 10 % to 90 % of the wingspan were employed, enabling a comprehensive assessment of the wake capture force distribution along the wingspan and throughout a flapping half-stroke.

It is clear that wing–wake interaction results in distinct effects across various spanwise locations. For most of the wing planform shapes, at the beginning of a flapping half-stroke, the sections in close proximity to the wingroot exhibit a negative wake capture force coefficient, whereas the sections closer to the wingtip show a pronounced positive wake capture force coefficient. As the wing advances through its stroke motion, a dual-peak pattern in normal force coefficient is found in the region near the wingtip, typically for wing planform shapes with $AR \geq 4$: following the initial peak in force coefficient near the

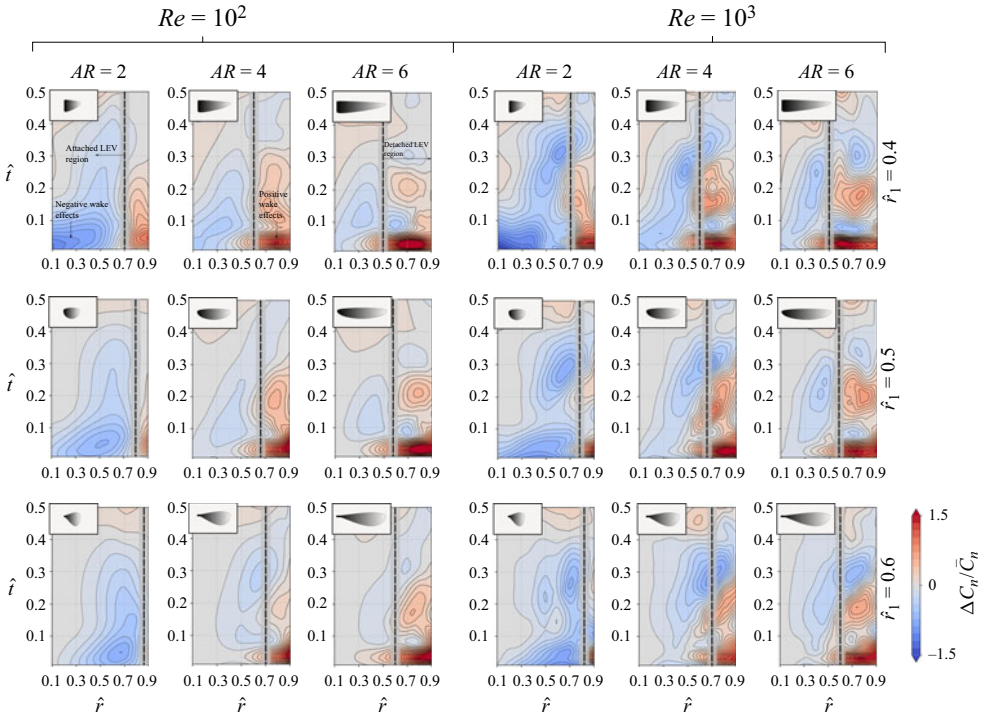

Figure 8. Normalised wake capture normal force coefficient distributions for different AR and $\hat{r}_1$ wings at $Re = 10^2$ and 10^3. The LEV detachment locations are indicated by the vertical dashed lines, with grey bars indicating uncertainty due to spanwise resolution in sectional assessment.

beginning of the half-stroke, there is a rapid decline to a trough at approximately $\hat{t} = 0.1$, succeeded by a subsequent increase leading to a second peak just before mid-half-stroke. However, following this second peak, a trough characterised by a negative wake capture effect typically ensues. On the other hand, the negative force coefficient closer to the wingroot tends to persist and extend further towards the wingtip as time progresses. Generally, the value of wake capture force coefficient tends to diminish over time, dwindling notably after the point of mid-half-stroke.

The shape of the wing planform shows significant influence on wake capture force production: with the increase in AR, the region associated with a positive wake capture force coefficient tends to extend within the region near the wingtip. On the other hand, with the increase in $\hat{r}_1$, primarily for the lower AR wings, the area of positive coefficient tends to diminish and covers a reduced region near the wingtip. This trend is consistent with the observed detachment locations of the LEV, which will be discussed next.

Figure 8 showcases the LEV spanwise detachment location for the different wing planform shapes, where the detachment location was obtained based on the interrogation window approach used to assess the circulation behaviour along the wingspan. A clear correlation between the wake capture force production and the detachment of the LEV is observed: on the inboard wing region where the LEV is attached, negative wake capture force production is generally observed (domination of blue colour within the contours), whereas on the outboard wing region experiencing a detached LEV, positive wake capture force production is observed (red colour within the contours emerges). Such correlation in force production and LEV detachment is supported by the observations of the wake

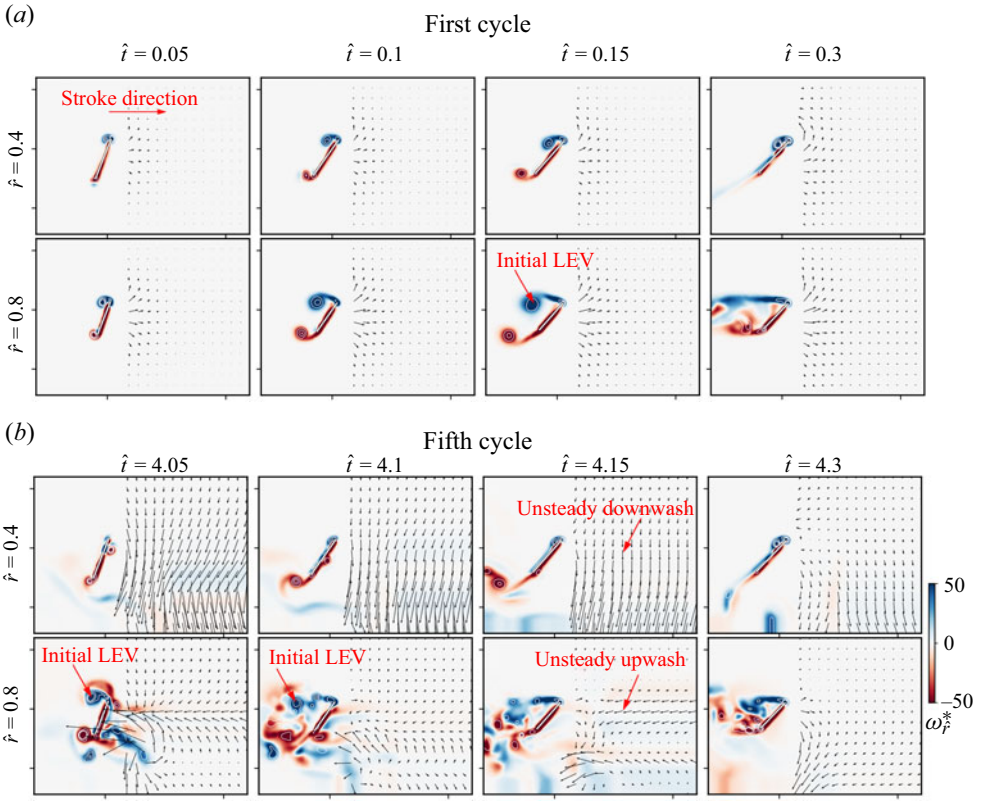

Figure 9. Comparison of sectional flow structures and velocity fields from the first and fifth cycles at $Re = 10^3$ for representative inboard and outboard wing sections of the wing planform with $AR = 4$ and $\hat{r}_1 = 0.5$. For clarity, flow field velocity vectors are not included beside the wing surface.

velocity fields presented in § 3.1, and demonstrated in figures 5–7, where an attached LEV results in an unsteady downwash field; whereas a detached LEV leads to an unsteady upwash field in the subsequent flapping half-stroke. Notably, the upwash associated with the detached LEV region will lead to a more rapid development of the LEV, hence early detachment of the initial LEV, demonstrated earlier in the 3-D flow visualisations shown in figures 4(*c*,*d*).

To further illustrate the previous point, figure 9 compares the sectional flows and velocity fields from the first and fifth cycles of the example wing case with $AR = 4$ and $\hat{r}_1 = 0.5$. In this demonstration, representatives of both the inboard and outboard wing sections are presented. It is clear that during the first stroke cycle, both wing sections travel in clean fields with no induced flow, but during the fifth stroke cycle, the inboard wing section travels in a downwash field whereas the outboard wing section travels in an upwash field formed due to the presence of the wake. For the inboard wing section, the unsteady downwash results in a reduced effective angle of attack, leading to a smaller LEV, which effectively prevents the detachment of the LEV within this region. On the other hand, for the outboard wing section, due to the unsteady upwash effect, the initial LEV quickly detaches near the beginning of the flapping half-stroke (at $\hat{t} = 4.1$; see also figures 4*c*,*d*). This detachment process is followed by the accumulation of the feeding vorticity from the leading edge resulting in subsequent development of the LEV. The more

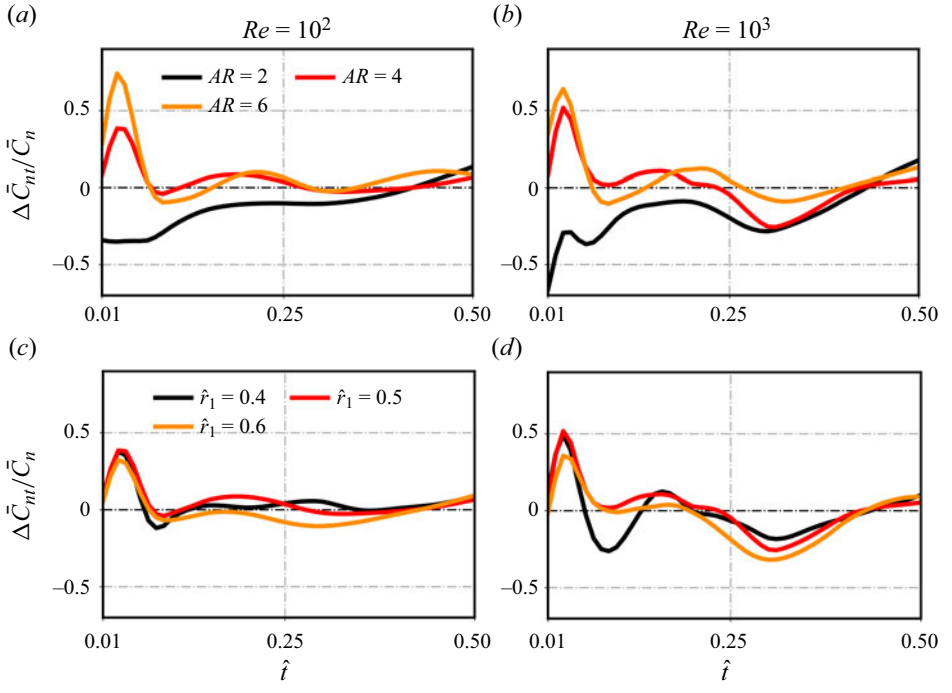

Figure 10. Normalised wake capture normal force coefficient variation throughout a flapping half-stroke at the two different Reynolds numbers simulated: (*a*,*b*) for different *AR*, and (*c*,*d*) for different $\hat{r}_1$ cases.

rapid development/shedding of the LEV within the outboard wing region provides clear explanation of the dual-peak pattern found in the wake capture force coefficients in figure 8. A strong momentary upwash at the beginning of the flapping half-stroke leads to the development of a stronger LEV, hence the first peak in the wake capture force coefficient. This is then followed by the rapid detachment of the initial LEV, leading to the sudden drop in wake capture force coefficient at approximately $\hat{t} = 0.1$. However, as the wing continues in its stroke motion, subsequent development of the LEV under the unsteady upwash field leads to the increased wake capture force production and hence the second peak observed in the force coefficient.

To further elucidate the wake capture force production, the normal force coefficients were averaged either over the wingspan or throughout a flapping half-stroke. Averaging over the wingspan reveals the distribution of wake capture force production throughout a flapping half-stroke, $\Delta\bar{C}_{nt}$, while averaging over time offers insight into its distribution along the wingspan, $\Delta\bar{C}_{ns}$. Figure 10 shows the force coefficient distributions throughout a flapping half-stroke for different wing planform shapes. For cases with varying *AR*, the $\hat{r}_1$ value was set at 0.5 (figures 10*a*,*b*), whereas for cases with varying $\hat{r}_1$, the *AR* was set at 4 (figures 10*c*,*d*). Figures 10(*a*,*b*) illustrate that the small aspect ratio wing ($AR = 2$) consistently shows negative wake capture force production. This is expected, as the small aspect ratio wing shows minimal LEV detachment, and the wing–wake interaction flow pattern is dominated by unsteady downwash. On the other hand, the higher aspect ratio wings show a dual-peak pattern in force production. The reason behind such a pattern, as explained above, is due to the unsteady upwash effect experienced by the outboard wing regions, leading to more rapid development and shedding of LEVs.

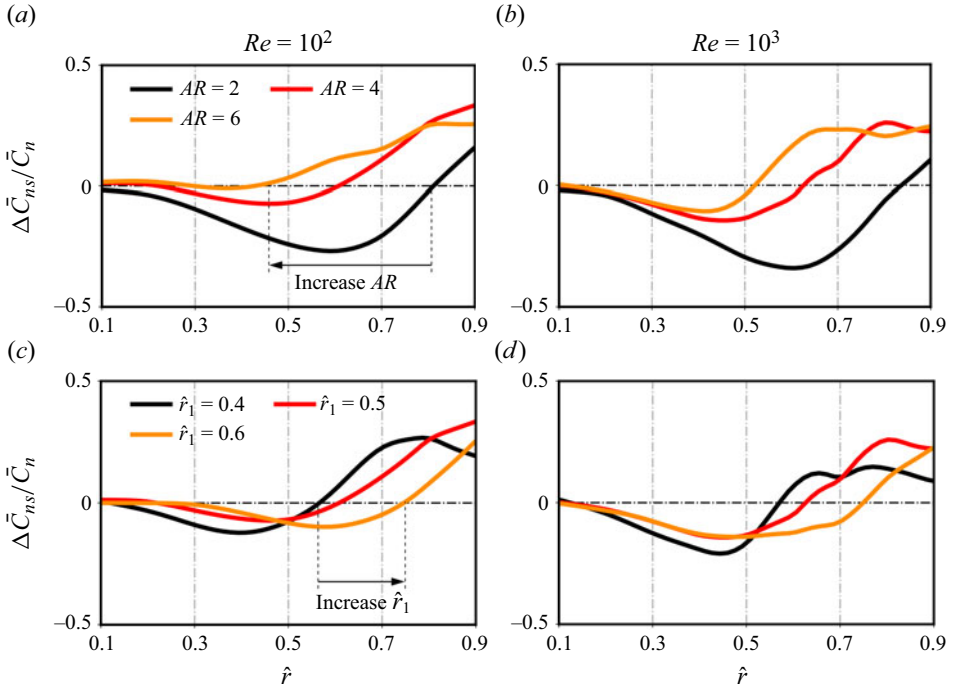

Figure 11. Normalised wake capture normal force coefficient variation along the wingspan at the two different Reynolds numbers simulated: (*a*,*b*) for different *AR*, and (*c*,*d*) for different $\hat{r}_1$ cases.

Figure 11 shows the wake capture force distribution along the wingspan, for the same wing planform shapes. A consistent distribution pattern emerges across all *AR* and $\hat{r}_1$ values: a small wake capture force coefficient is evident near the wingroot, which decreases to negative values as the radial distance from the wingroot ($\hat{r}$) increases and reaches a trough, typically within the range $\hat{r} = 0.3$–0.7. As $\hat{r}$ increases further, the normal force coefficient recovers and becomes positive up to the wingtip. Notably, the spanwise location where the transition occurs from negative to positive force coefficient moves inboard towards the wingroot as the aspect ratio increases, whereas the spanwise transition location moves outboard towards the wingtip as $\hat{r}_1$ increases. These demonstrations further confirm the positive role of the LEV detachment on wake capture force production: both increasing *AR* and/or decreasing $\hat{r}_1$ lead to an increased LEV detachment region near the wingtip, which consistently aligns with the increased region of positive wake capture force coefficients.

Figure 12 shows the correlation between the normalised average wake capture normal force coefficient against both the LEV detachment location and the wing aspect ratio. The data used to create these correlation plots include the results already presented for the wing planform shapes (with aspect ratios 2, 4 and 6, and centroid locations 0.4, 0.5 and 0.6) at both Reynolds numbers. Evidently, whilst figure 12(*a*) shows a strong negative correlation between the detachment location of the LEV and wake capture force production, figure 12(*b*) shows a highly positive correlation between wake capture force production and the wing aspect ratio. These results further showcase the positive role of LEV detachment on wake capture force production: a more extended LEV detachment region results in higher wake capture force coefficients.

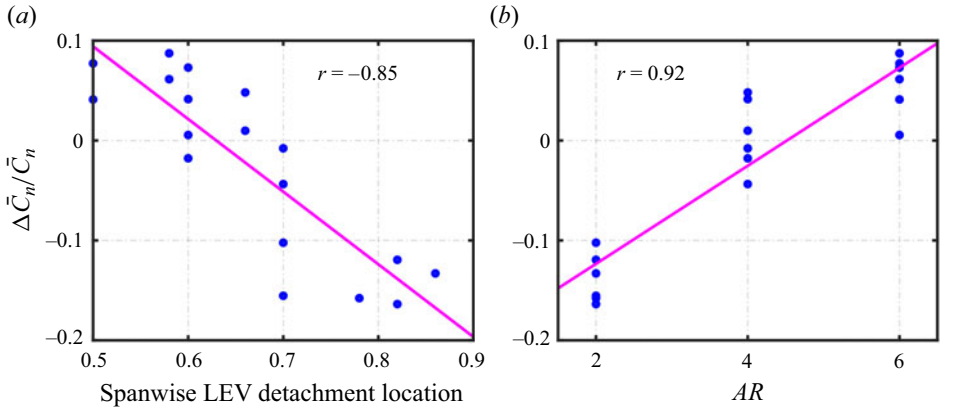

Figure 12. Correlation between the normalised average wake capture normal force production against (*a*) LEV detachment location, and (*b*) aspect ratio. Least squares fits are shown as purple lines, where r is the Pearson correlation coefficient (Freedman, Pisani & Purves 2007).

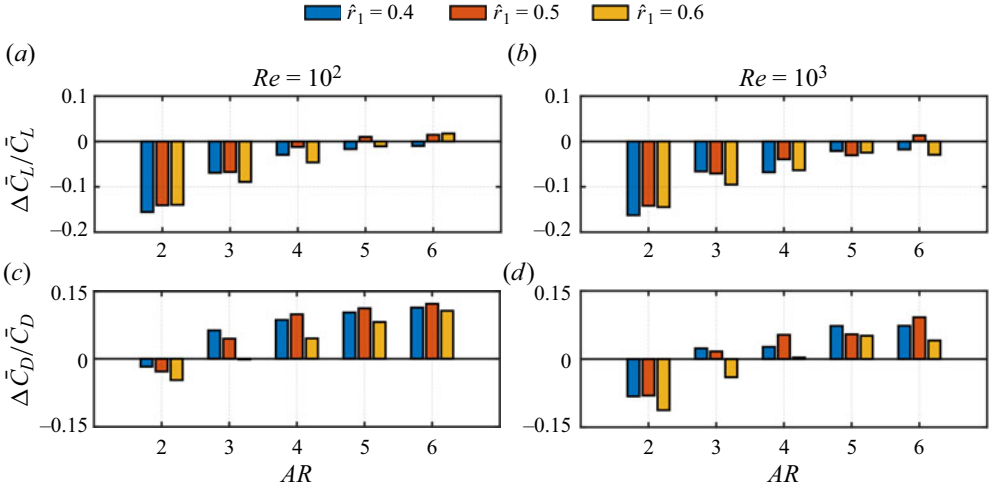

Figure 13. Normalised mean wake capture lift and drag coefficients for all aspect ratio and radial centroid locations investigated.

Finally, we conclude this section by presenting the mean lift and drag coefficients due to wake capture effects. Figure 13 shows the mean wake capture lift and drag coefficients $\Delta\bar{C}_L$ and $\Delta\bar{C}_D$ normalised by the mean lift and drag coefficients of the fifth cycle, $\bar{C}_L$ and $\bar{C}_D$. These results, for the symmetric half-stokes kinematics adopted in this study, show that in general, wake capture leads to a reduction in total lift and an increase in total drag. However, as the aspect ratio increases, the reduction in lift becomes increasingly mitigated, but the associated drag keeps increasing with the increase in aspect ratio. This trend in lift and drag production against aspect ratio agrees with our previous observations, where an increase in aspect ratio leads to extended region of LEV detachment, hence a more significant unsteady upwash effect on the outboard wing region. Note that although a generally reduced wake capture lift is found in the current study, our results imply that by effectively modulating the conditions on the outboard wing region (where the unsteady

upwash effect leads to an increased force production), enhanced aerodynamic performance may be obtained.

4. Concluding remarks

The results presented in this work clearly underscore the substantial influence of the spanwise variation of the wake structures on wake capture force production. In fact, a consistent pattern emerged across all investigated wing planform shapes: on the inboard wing region where an attached LEV structure is evident, wing–wake interaction results in negative force production, whereas on the outboard wing region near the wingtip, that is typically experiencing detachment of LEV, wing–wake interaction leads to positive force production. For the inboard wing region, the wing travels backwards into its wake under a downward induced velocity field, i.e. unsteady downwash effect, leading to a reduction in the effective angle of attack during the subsequent flapping half-stroke, consequently reducing aerodynamic force production. On the contrary, for the outboard wing region, an unsteady upwash effect emerges due to the wake velocity field directed towards the wing surface, resulting in a more rapid development and shedding of the LEV during the subsequent half-stroke, significantly increasing force production near the beginning of the stroke motion. This becomes particularly pronounced in cases involving wings with a large aspect ratio or a small radial centroid location, for which the detachment of the LEV extends over a larger area within the wingtip region.

Throughout a stroke cycle, the LEV formed on flapping wings remains attached for a substantial portion of the wingspan, effectively preventing stall. This significance of LEV attachment is well established due to its pivotal role in augmenting lift generation during flapping wing translation. However, stall can occur, primarily in the region near the wingtip. This susceptibility to stall at the wingtip region arises either from a radial constraint imposed by the Rossby number, where the LEV becomes unstable beyond a certain radial distance from the wingroot (Lentink & Dickinson 2009; Kruyt *et al.* 2015; Lee, Lua & Lim 2016; Broadley & Nabawy 2023), or as a result of interactions between the LEV and the shedding of vortices originated from the wingtip – a consequence of the finite wingspan. The present study reveals that although an attached LEV enhances lift production during the wing's translational motion, its associated wing–wake interaction results in detrimental wake capture aerodynamic force production. In contrast, although a detached LEV near the wingtip diminishes lift during the wing's translational motion, its associated wake capture aerodynamic force production within this region is positive.

Finally, it should be noted that the current study has focused on the effects of wing planform and Reynolds number on the wake capture problem. This is because these variables are believed to be the main influencers on the LEV structures of a flapping wing. Whilst the employed kinematics in this study are representative of normal hovering flight of insects, it should be recognised that there are other kinematic variables such as the pitching phase and deviation angle that are important to insect wing aerodynamics, and their effects should be considered in future studies.

Funding. The authors are grateful to the Leverhulme Trust for funding this work through Research Project Grant RPG-2019-366.

Declaration of interests. The authors report no conflict of interest.

Author ORCIDs.
Hao Li https://orcid.org/0000-0002-8726-7976;
Mostafa R.A. Nabawy https://orcid.org/0000-0002-4252-1635.

References

Baik, Y.S., Bernal, L.P., Granlund, K. & Ol, M.V. 2012 Unsteady force generation and vortex dynamics of pitching and plunging aerofoils. *J. Fluid Mech.* **709**, 37–68.

Berman, G.J. & Wang, Z.J. 2007 Energy-minimizing kinematics in hovering insect flight. *J. Fluid Mech.* **582**, 153–168.

Birch, J.M. & Dickinson, M.H. 2003 The influence of wing–wake interactions on the production of aerodynamic forces in flapping flight. *J. Expl Biol.* **206** (13), 2257–2272.

Broadley, P. & Nabawy, M.R.A. 2023 On the validity of the normal force model for steadily revolving wings: an experimental investigation. *Aerospace* **10** (5), 388.

Broadley, P., Nabawy, M.R.A., Quinn, M.K. & Crowther, W.J. 2022 Dynamic experimental rigs for investigation of insect wing aerodynamics. *J. R. Soc. Interface* **19** (191), 20210909.

Dickinson, M.H. & Götz, K.G. 1993 Unsteady aerodynamic performance of model wings at low Reynolds numbers. *J. Expl Biol.* **174**, 45–64.

Dickinson, M.H., Lehmann, F.O. & Sane, S.P. 1999 Wing rotation and the aerodynamic basis of insect flight. *Science* **284** (5422), 1954–1960.

Ellington, C.P. 1984*a* The aerodynamics of hovering insect flight. 2. Morphological parameters. *Phil. Trans. R. Soc. Lond.* B **305** (1122), 17–40.

Ellington, C.P. 1984*b* The aerodynamics of hovering insect flight. 3. Kinematics. *Phil. Trans. R. Soc. Lond.* B **305** (1122), 41–78.

Freedman, D., Pisani, R. & Purves, R. 2007 *Statistics (International Student Edition)*, 4th edn. WW Norton & Company.

Harbig, R.R., Sheridan, J. & Thompson, M.C. 2013 Reynolds number and aspect ratio effects on the leading-edge vortex for rotating insect wing planforms. *J. Fluid Mech.* **717**, 166–192.

Hunt, J.C.R., Wray, A.A. & Moin, P. 1988 Eddies, streams, and convergence zones in turbulent flows. In *Proceedings of the Summer Program in Center for Turbulence Research*, pp. 193–208.

Issa, R.I. 1986 Solution of the implicitly discretised fluid flow equations by operator-splitting. *J. Comput. Phys.* **62** (1), 40–65.

Jardin, T. 2017 Coriolis effect and the attachment of the leading edge vortex. *J. Fluid Mech.* **820**, 312–340.

Jones, A.R. & Babinsky, H. 2011 Reynolds number effects on leading edge vortex development on a waving wing. *Exp. Fluids* **51** (1), 197–210.

Kruyt, J.W., Van Heijst, G.J.F., Altshuler, D.L. & Lentink, D. 2015 Power reduction and the radial limit of stall delay in revolving wings of different aspect ratio. *J. R. Soc. Interface* **12** (105), 1–7.

Lee, Y.J. & Lua, K.B. 2018 Wing–wake interaction: comparison of 2D and 3D flapping wings in hover flight. *Bioinspir. Biomim.* **13** (6), 066003.

Lee, Y.J., Lua, K.B. & Lim, T.T. 2016 Aspect ratio effects on revolving wings with Rossby number consideration. *Bioinspir. Biomim.* **11** (5), 056013.

Lentink, D. & Dickinson, M.H. 2009 Rotational accelerations stabilize leading edge vortices on revolving fly wings. *J. Expl Biol.* **212** (16), 2705–2719.

Li, H. & Nabawy, M.R.A. 2022*a* Capturing wake capture: a 2D numerical investigation into wing–wake interaction aerodynamics. *Bioinspir. Biomim.* **17** (6), 066015.

Li, H. & Nabawy, M.R.A. 2022*b* Effects of stroke amplitude and wing planform on the aerodynamic performance of hovering flapping wings. *Aerospace* **9** (9), 479.

Li, H. & Nabawy, M.R.A. 2022*c* Wing planform effect on the aerodynamics of insect wings. *Insects* **13** (5), 459.

Nabawy, M.R.A. 2023 A simple model of wake capture aerodynamics. *J. R. Soc. Interface* **20** (206), 20230282.

Nabawy, M.R.A. & Crowther, W.J. 2015 Aero-optimum hovering kinematics. *Bioinspir. Biomim.* **10** (4), 44002.

Patankar, S.V. & Spalding, D.B. 1972 A calculation procedure for heat, mass and momentum transfer in three-dimensional parabolic flows. *Intl J. Heat Mass Transfer* **15** (10), 1787–1806.

Phillips, N., Knowles, K. & Bomphrey, R.J. 2015 The effect of aspect ratio on the leading-edge vortex over an insect-like flapping wing. *Bioinspir. Biomim.* **10** (5), 056020.

Rival, D.E., Kriegseis, J., Schaub, P., Widmann, A. & Tropea, C. 2014 Characteristic length scales for vortex detachment on plunging profiles with varying leading-edge geometry. *Exp. Fluids* **55** (1), 1–8.

Sun, M. & Du, G. 2003 Lift and power requirements of hovering insect flight. *Acta Mechanica Sin.* **19** (5), 458–469.

Sun, M. & Tang, J. 2002 Unsteady aerodynamic force generation by a model fruit fly wing in flapping motion. *J. Expl Biol.* **205** (1), 55–70.